Shock Waves
DOI 10.1007/s00193-018-0815-3

ORIGINAL ARTICLE

Some issues for blast from a structural reactive material solid

F. Zhang[1]

Received: 10 September 2017 / Revised: 23 January 2018 / Accepted: 30 January 2018

Abstract Structural reactive material (SRM) is consolidated from a mixture of micro- or nanometric reactive metals and metal compounds to the mixture theoretical maximum density. An SRM can thus possess a higher energy density, relying on various exothermic reactions, and higher mechanical strength and heat resistance than that of conventional CHNO explosives. Progress in SRM solid studies is reviewed specifically as an energy source for air blast through the reaction of fine SRM fragments under explosive loading. This includes a baseline SRM solid explosion characterization, material properties of an SRM solid, and its dynamic fine fragmentation mechanisms and fragment reaction mechanisms. The overview is portrayed mainly from the author's own experimental studies combined with theoretical and numerical explanation. These advances have laid down some fundamentals for the next stage of developments.

Keywords Structural reactive material · Reactive material · Intermetallics · Thermite · Metal combustion · Blast · Reactive fragment

1 Introduction

The possibility of shock-induced reaction in metal-based reactive materials, in the form of a powder mixture, appeared in 1956 in the Russian literature and gave rise to a large body of work thereafter [1–4]. This has resulted in advances in solid-state chemistry under high-pressure shock loading down to microscopic scales involving defect mechanisms. As a new branch of reactive materials which emerged around 2000s, a structural reactive material (SRM) is defined to be comprised of a mixture of micrometric or nanometric energetic metals and metal compounds, consolidated to its theoretical maximum density (TMD). An SRM thus bears both macroscale continuum solid properties (density, energy, mechanical strength, etc.) and mesoscale properties of reactivity and dissimilarity (e.g., interface discontinuities in impedance, hardness, etc.), as shown in Fig. 1. Depending on component morphologies, an SRM solid structure can adopt a granular, laminate, fiber, or other configurations [5–16]. As a growing area for innovative materials, SRMs have a wide application potential, including armament systems, reactive armors, energy sources for outer space uses through intermetallic reactions, and for air blast through oxidation of fine fragments of an SRM solid under explosive loading. The latter will be the main focus of the present paper.

Filler was perhaps the first to report the influence of a reactive casing (prepared from a bulk zirconium solid) on air blast under explosive loading in 1985 [17]. Studies on air blast augmentation from an SRM casing were initiated in the early 2000s, in which mechanical strength has been considered as important as the energy supplemented from the casing, see for example, [6,8,9,13–16].

One of the key parameters for an SRM-cased explosive charge was the casing-to-explosive mass ratio, M/C [13]. As a baseline SRM solid, explosively loaded aluminum (Al) casing delivered free-field blast enhancement only with small M/C values, owing to their fine fragment combustion. Little augmentation to air blast has been observed in the free field for thick Al casings in which $M/C \geq 1.75$, where the majority of primary fragments were relatively large and thus functioned as inert material only. Significant blast enhance-

Communicated by P. Hazell.

✉ F. Zhang
fan.zhang@drdc-rddc.gc.ca

[1] Defence Research and Development Canada, P.O. Box 4000, Station Main, Medicine Hat, AB T1A 8K6, Canada

Published online: 21 March 2018

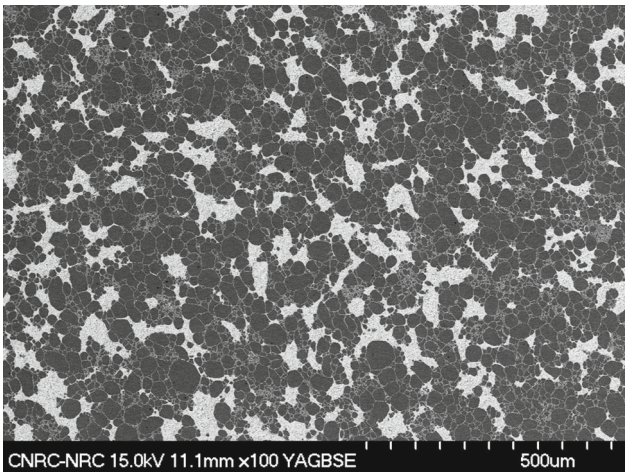

Fig. 1 Scanning electronic micrograph for hot isostatic pressed 10Al+MoO_3 showing both bulk properties (TMD and strength) and mesoscale dissimilarity. Al is in dark gray and MoO_3 in light gray [16]

ment from thick casings was observed mostly in confined environments through high-speed fragment impact on a target, in which resulting secondary or tertiary fine fragments reacted with the detonation products and air. Additional mechanisms must therefore be sought in order to create a large number of primary fine fragments for more efficient energy release from casings of large M/C values.

How fine the fragments should be for effective energy release in detonation products or air largely depends on materials involved in an SRM solid. For an Al particle suspension, its detonation in air requires particle sizes within a few micrometers, and its rapid deflagration in detonation products and air needs particles within a few tens of micrometers [18–22]. Regarding fragmentation mechanisms, the porosity of a reactive material mixture does promote fine fragmentation. Large porosity, however, results in a deficit in TMD, thus leading to low mechanical strength [23], which is in opposition with the definition of an SRM solid. Reactive composites, made of reactive metal particles with a low melting point or low yield strength binder such as polytetrafluoroethylene (PTFE) or casting resins (polyester, epoxy, and polyurethane), generate grain-scale fine metal fragments for effective fluoridation, oxidation, etc. [24–26]. This class of composites, however, yields a low tensile strength in general even when they are prepared to reach full TMD.

For a full TMD high-strength SRM solid, fine fragmentation mechanisms have been proposed based on the intrinsic mesoscale properties of dissimilarity and reactivity. In a structural discontinuity mechanism [6–9,12,14], the grain-scale discontinuities in impedance mismatch, hardness, etc., dominate at dissimilar ingredient interfaces within an SRM solid. Near the interfaces, shock dynamics results in local high temperatures, normal/shear stresses and deformation and, later, different accelerations from dissimilar inertia, leading to fine fragments. In a reactive-hot-spot mechanism [15,16], micrometric reactive material particles are distributed in a fuel-rich SRM solid. Their intermetallic reactions under explosive loading creates heat and gas products to form mesoscale hot spots, which initiate local fractures leading to fine SRM fragments.

A high detonation pressure increases the strain rate of casing material under explosive loading, resulting in smaller fragment sizes according to Grady's dynamic fragmentation theory [27,28]. In the case of an SRM solid casing, high shock loading generates large discontinuities in strain and strain rate at the grain interfaces, thus promoting fine fragmentation. As for intermetallic or thermite reaction within an SRM solid, both shock initiation pressure and sufficient gas products are necessary criteria in choosing a reactive material which favors hot spot fine fragmentation. Gas products can be estimated from thermochemical equilibrium calculations validated with experimental data [29,30]. The shock initiation pressure can be determined by plate impact experiments [31]. Ignition temperature is another key parameter for intermetallic reaction within an SRM solid. In a vacuum experimental study [32], ignition temperatures were found to be similar for arrested-reactive-milled nanocomposites $2Al \cdot 3CuO$, $4Al \cdot Fe_2O_3$, $8Al \cdot MoO_3$, and $2.35Al \cdot Bi_2O_3$ in the range of 800–950 K, which is in the vicinity of the Al melting point. The study also suggested the likelihood of low-temperature redox reactions occurring prior to ignition and prone to rapid decomposition upon further heating.

The reaction mechanisms of SRM fragments in air or oxidizing gases depend not only on the composition but also strongly on the fragment size distribution. From the viewpoint of explosion performance, the SRM fragment reaction mechanisms may be divided into two categories, namely detonation shock-induced reaction (DSIR) and target impact-induced reaction (IIR) [33–35]. IIR is dominant for a fragment distribution with a considerable mass fraction comprising large sizes, whereby secondary fragmentation upon impact on a hard target generates a large number of fine fragments whose prompt reaction provides enhanced blast loading near the target. For a distribution with a high mass fraction of micrometric size fragments, reaction of the fine primary fragments takes place promptly following explosive detonation (i.e., DSIR). In this case, the expanding fragments continuously react and supplement energy which enhances the primary blast as it propagates. Hence, recovery of initial fragmentation characters before they have been altered by early reaction or by subsequent impact is essential for a better understanding of blast performance of an SRM solid.

This paper provides a review mainly from the author's own studies on the above-mentioned aspects with respect to the heterogeneous blast from a high-strength SRM solid under explosive loading. The paper first presents the basic SRM blast characterizations using a baseline Al solid (Sect. 2),

followed by a description of the physical and chemical properties required for a high-strength SRM solid made of various metal elements and compounds (Sect. 3). Its dynamic fine fragmentation mechanisms are then described in order for prompt energy release from the solid to occur (Sect. 4). Finally, the SRM fragment reaction mechanisms are portrayed from the point of view of explosion and blast performance (Sect. 5). In the paper, the properties are mostly addressed with respect to SRM, instead of reactive material in general. Over a hundred SRM samples have been tested in the past years; only selected examples are reviewed in an attempt to describe more fundamental issues observed from the large number of tests. From the nature of the work, this paper will touch on various different subject areas (shock dynamics in microstructures, reaction in reactive materials, fragmentation, dense reactive particle flow, heterogeneous blast, confinement effects, etc.) and integrate them to explore how an SRM solid can be used as an effective blast source. A thorough treatise on these subject areas lies beyond the scope of this paper; the reader is referred to more comprehensive sources in the literature that may be consulted with respect to the specific topics, for example, in [4,21,36–39].

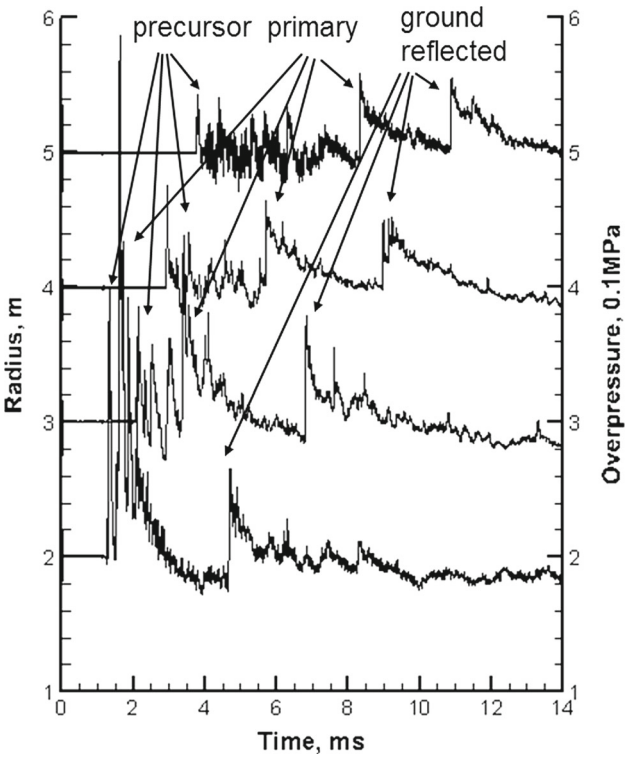

Fig. 2 Blast pressure histories along the radius from an $M/C = 1.75$ Al-cased C4 charge with $C = 2$ kg [13]

2 Blast from a baseline SRM solid

2.1 Free-field blast

The 6061-T6 Al has been selected to be the baseline SRM solid, whose performance is comparable to a full TMD solid made of micrometric Al particles. The blast wave structure from the baseline SRM-cased explosive charge in the near field is characterized by a double-shock front structure, where a precursor shock wave travels ahead of the primary blast [13]. Figure 2 displays pressure histories along the radius from a cylindrical Al-cased composition C4 charge (91 wt% RDX with a detonation velocity $D = 8000$ m/s), detonated from the charge top with the charge center 1.6 m from the ground. The cased charge has a casing-to-explosive mass ratio of $M/C = 1.75$ and a ratio of casing length to inner diameter: $L/2R_I = 1.6$ ($C = 2$ kg, $2R_I = 101.6$ mm). The pressure transducers positioned at the radii of 2, 3, 4, and 5 meters are mounted on lollipop stands at the same height as that of the charge center.

In Fig. 2, the precursor shock wave starts to emerge from the primary shock front at 2 m. In the subsequent propagation, the precursor shock wave features a number of pressure peaks associated with ballistic air shocks attached to fragment clusters that traverse the primary blast front. Note that in Fig. 2 the last wave front in each pressure history is from the ground-reflection. While the primary blast wave expands and continuously decays, the precursor front propagates with a very mild deceleration owing to the fragment inertial motion. The fragment number density, however, decreases following the expansion. As a result, the precursor shock wave widens during the propagation, accompanied with an increase in period between peaks and a decrease in their amplitude. Noting that the precursor shock originates in an assembly of bow shocks from the casing fragments whose spatial distribution is stochastic, the precursor shock shape and peaks vary in every direction and are not repeatable.

A maximum impulse, which includes both precursor shock and primary blast loading, is integrated from the precursor shock front to the point before the ground-reflected shock front in the pressure history. The maximum impulse is used to evaluate an SRM-cased blast as shown in Fig. 3. The results, in comparison with that from a steel-cased C4 charge of the same M/C, indicate that the maximum impulse from the Al-cased charge exhibits an increase only at the very near field within a blast propagation distance of 40–50R_I, and thereafter becomes identical with that from the steel-cased charge. This would suggest that the majority of primary Al fragments are relatively large and thus functioned as inert material.

A distribution of Al casing fragment sizes in mass and number, recovered at 2 m radius in an arena arrangement, shifts toward smaller sizes with a larger number density when compared with that of steel at the same ratio of $M/C = 1.75$.

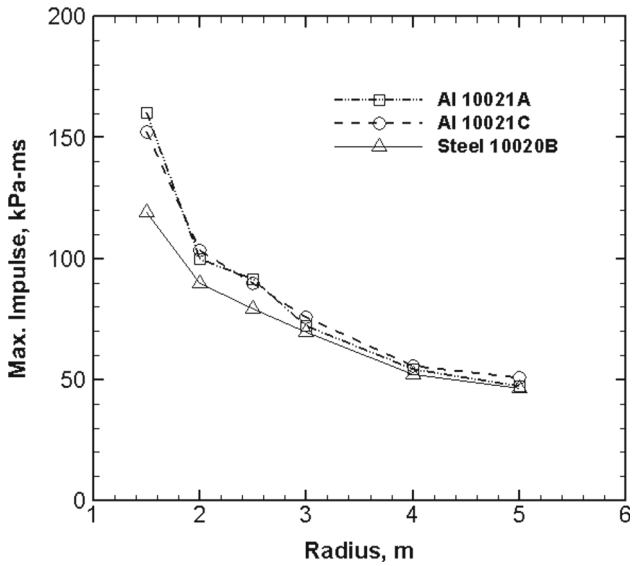

Fig. 3 Maximum impulses including precursor shock and primary blast for $M/C = 1.75$ Al-cased and steel-cased C4 charge with $C = 2$ kg

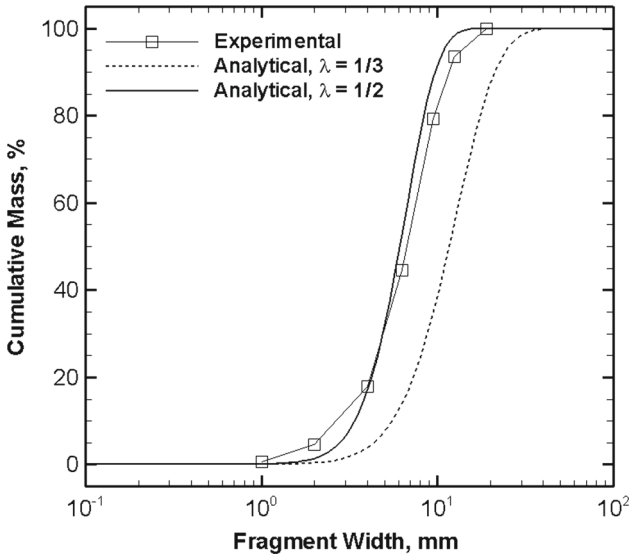

Fig. 4 Analytical Al fragment distribution compared with the experiment at $M/C = 1$ [13]

The fine Al fragments burned within 2 m radius cannot be detected in such a standard arena test.

Considering that the Al dynamic fragmentation bears similarity to that from a ductile mild steel casing, Grady's energy-governed dynamic fragmentation theory for a nominal fragment width, S, is applied to the Mott probability curve [27,28,36,40]:

$$S = \psi \dot{\varepsilon}^{-2/3}, \quad \psi = \left(12K_{\mathrm{f}}^2/\rho E\right)^{1/3}, \tag{1}$$

$$N(>m) = \exp\left[-(m/\mu)^{\lambda}\right], \tag{2}$$

which are closed by defining a strain rate [13]:

$$\dot{\varepsilon} = V_{\mathrm{G}}/R_{\mathrm{f}} \tag{3}$$

In (1)–(3), $\dot{\varepsilon}$ is the circumferential strain rate and parameter ψ is associated with the energy dissipated by tensile fracture. K_{f}, ρ, and E are casing dynamic fracture toughness, material density, and elastic modulus, respectively. $N\ (>m)$ is the cumulative number of fragments with a mass greater than m, where 2μ is a mean fragment mass $2\mu = \rho S^3$. In Mott's analysis, the statistical distribution parameter $\lambda = 1/2$ is most appropriate for thin casings and $\lambda = 1/3$ is for thick casings. V_{G} is the Gurney velocity representing a maximum cylindrical casing expansion velocity and R_{f} is casing failure radius. Hutchinson's improved fragment momentum is used to obtain V_{G} and R_{f} [13,41].

Figure 4 plots analytical fragment distributions from (1)–(3) for the Al casing ($M/C = 1$), showing promise in comparison with the experiment. It is noticeable that the fragmentation described in equation (1) is based on tensile fracture where failure proceeds by crack propagation. Alternative equations must be used when the dynamic fracture toughness is high or shear fracture becomes dominant.

2.2 Confined blast

Confined experiments have been conducted in a 23 m^3 cylindrical steel chamber, 3 m internal diameter (ID) $\times$ 3.25 m length in a horizontal configuration [42]. An Al-cased cylindrical charge is suspended vertically in the chamber center and detonated from the charge top.

Figure 5 gives examples of the long-time reverberating pressure wave histories, due to shock-wall interactions, measured on the cylindrical wall, from 2 kg C4 charges with a 101.6 mm casing inner diameter at various M/C. An increase in M/C results in a decrease in initial explosion pressure but an increase in the follow-on pressure. At $M/C = 1.75$, within the first 10 ms between the first and fourth reflections on the chamber wall, the pressure rise for the Al-cased charge achieves a factor of 1.5 versus the bare charge and a factor of 2.2 versus the steel-cased charge. This indicates rapid combustion of a considerable amount of fine fragments generated by secondary and tertiary fragmentation through wall impact and aerodynamic breakup (stripping and shattering) of molten fragments at high explosion temperature in the chamber [43]. Finally, the pressure approaches a quasi-static overpressure (QSP). At $M/C = 1.75$, the QSP for the Al-cased charge reaches a factor of 1.9 versus the bare charge and a factor of 2.4 over the steel-cased charge.

The QSP value is a long-time asymptotic solution of a closed reactive system in a constant volume chamber ($\mathrm{d}v = 0$). From the first law of thermodynamics, one obtains

$$\Delta p_{\mathrm{ex}} = p_{\mathrm{ex}} - p_0 = (\gamma - 1)mq/V \tag{4}$$

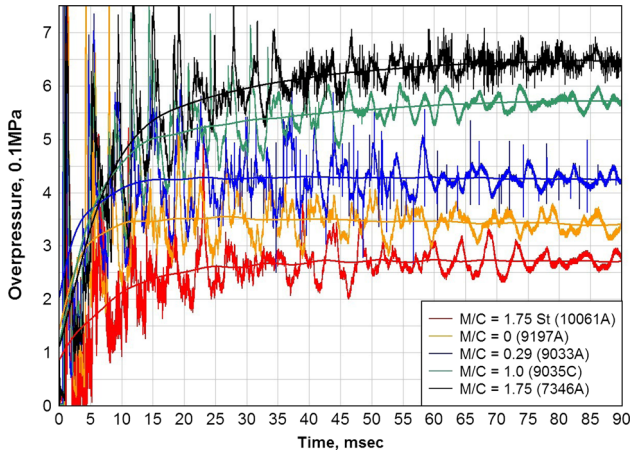

Fig. 5 Pressure histories from Al-cased 2 kg C4 charges at various M/C in a 23 m^3 chamber, with the red curve for $M/C = 1.75$ steel-cased charge [13]

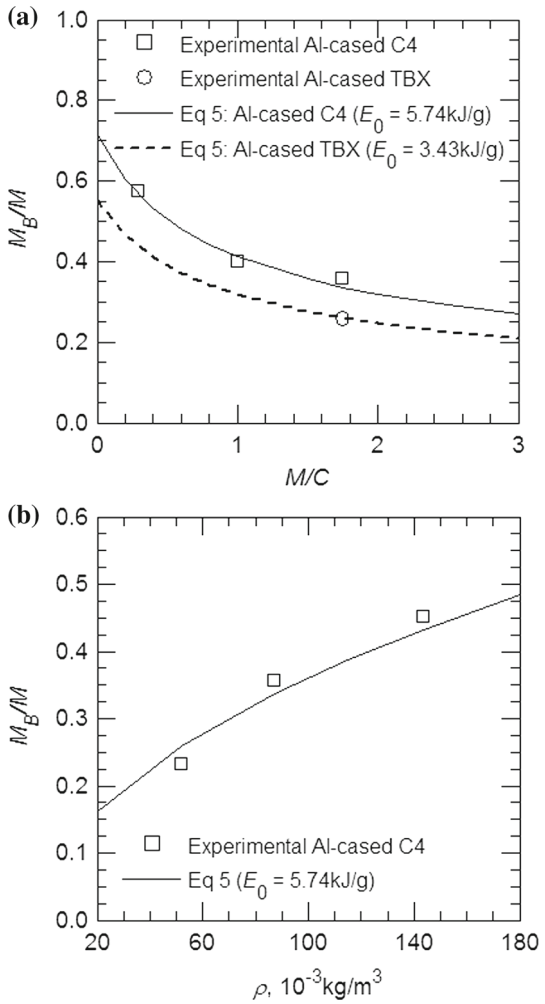

Fig. 6 Burnt casing mass fraction versus M/C and E_0 at $\rho = 86.96\,\mathrm{g/m^3}$ (**a**), and versus ρ at $M/C = 1.75$ and $E_0 = 5.74\,\mathrm{kJ/g}$ (**b**)

under ideal gas conditions. In (4), p_{ex}, p_0, γ, m, q, and V are the explosion pressure, initial pressure, isentropic index, total mass of the reactive system, heat release per mass of the reactive system, and the chamber volume, respectively. Thus, the explosion overpressure, Δp_{ex}, is proportional to the total explosion energy of the reactive system and therefore a quantity representing the magnitude of the explosion energy of a reactive system in a closed volume. More accurate theoretical explosion overpressure can be obtained from the equilibrium constant volume combustion calculation under the condition that a reactive system is perfectly mixed at the molecular level. Experimentally, the explosion overpressure is measured as a long-time QSP in a closed chamber. The deviation of the QSP from the theoretical prediction reflects the quality of mixing and the degree to which afterburning is complete under the adiabatic condition.

The burnt mass of a reactive material casing can be derived from the equilibrium constant volume explosion calculations by equaling the theoretical explosion overpressure with the experimental QSP, $\eta \Delta p_{ex} = \mathrm{QSP}$, with a casing material afterburning efficiency $\eta \leq 1$. The afterburning efficiency can also be examined in agreement with the mass of fragments and solid products recovered from the closed chamber. For the cylindrical cased charge testing configuration in the 23 m^3 chamber, $\eta = 0.85$. Figure 6 plots the obtained burnt casing mass ratio M_B/M, averaged over repeated tests, in terms of M/C, explosive type (i.e., detonation mechanical energy E_0) and the explosive loading density in the chamber $\rho = C/V$, where V is the chamber volume. The burnt casing mass ratio increases as the M/C decreases, or as E_0 or ρ increases.

A simple correlation of the experimental data in [13] further expresses that the burnt casing mass is proportional to the Gurney velocity and a square root of the loading density:

$$M_B/M = f(V_G(M/C, E_0), \rho) = \sigma \rho^{1/2} V_G \tag{5}$$

with the cylindrical Gurney velocity equation, where the Gurney energy $E_G \approx E_0$. In (5), $\sigma = 5.05 \times 10^{-4}\ \mathrm{s\,m^{1/2}\,kg^{-1/2}}$ is a fitting coefficient. The simple correlation equation (5) gives remarkable agreement with complex experimental results as indicated in Fig. 6.

Internal explosions of an Al-cased charge follow a scaling rule. For two cylindrical explosion chambers with volumes V_1 and V_2, the same QSP and the same scaled equilibrating time, τ_E, required for approaching QSP hold:

$$\mathrm{QSP} = \mathrm{QSP}_1 = \mathrm{QSP}_2, \quad \tau_E = t_{E1}/V_1^{1/3} = t_{E2}/V_2^{1/3} \tag{6}$$

if

$$M/C = M_1/C_1 = M_2/C_2, \quad \rho = C_1/V_1 = C_2/V_2 \tag{7}$$

The scaling rule has been validated in a 3 m ID, $V_1 = 23\,\mathrm{m^3}$ and an 1.18 ID, $V_2 = 2.1\,\mathrm{m^3}$ cylindrical steel

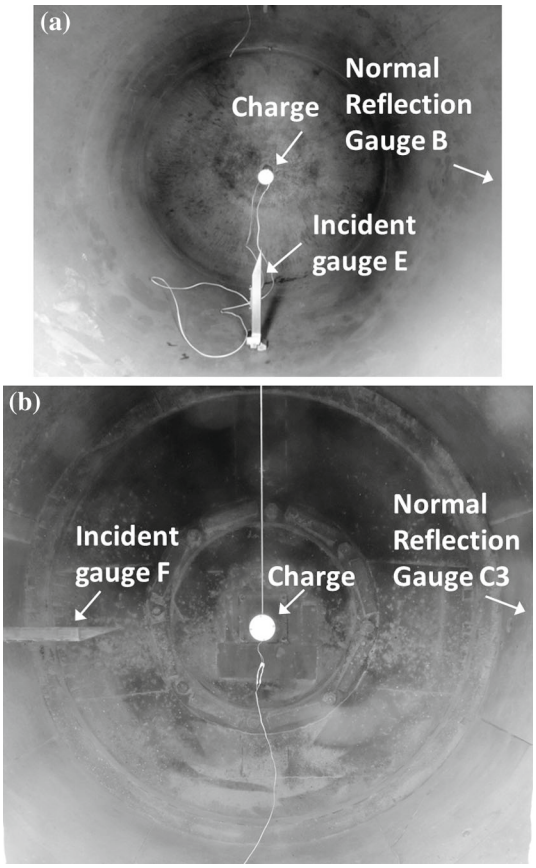

Fig. 7 Cylindrically symmetric test configurations. **a** 1.18 m ID, 2.1 m^3 chamber. **b** 3 m ID, 23 m^3 chamber

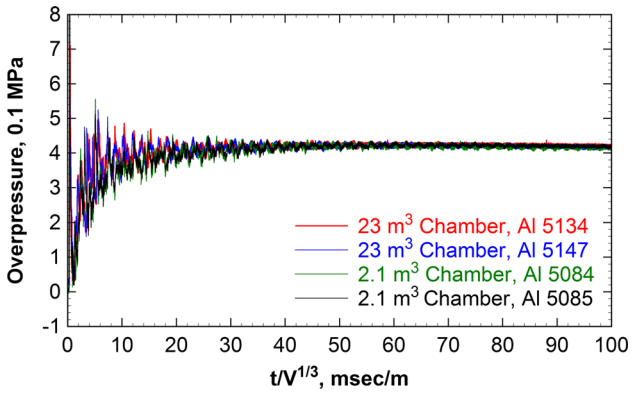

Fig. 8 Scaled pressure histories from two Al-cased 1.2 kg C4 charges in a 23 m^3 chamber and two Al-cased 0.11 kg C4 in a 2.1 m^3 chamber, with $M/C = 1.77$

chamber (Fig. 7), using cylindrical Al-cased C4 charges of $C_1 = 1.2\,\text{kg}$, $2R_{I1} = 76.2\,\text{mm}$; $C_2 = 0.11\,\text{kg}$, $2R_{I2} = 33.5\,\text{mm}$ in a cylindrical symmetry arrangement. This results in $\rho \approx 52\,\text{g/m}^3$ and $M/C = 1.77$ with the casing masses used, and the explosion results displayed in Fig. 8 validates (6). The internal explosion scaling rule provides a baseline in designing subscale experiments before moving to large scale testing.

3 Properties of an SRM solid

Physical and chemical properties of an SRM solid are largely governed by composition, mesoscale morphology, and a metallurgy consolidation approach.

The first step to construct an SRM may be to select a mixture composition to achieve a specific TMD and theoretical energy content. A large number of elemental metals in the periodic table can be considered to be components of an SRM solid, such as Li, Mg, B, Al, Ti, Zr, Zn, Mn, Fe, Nb, Ni, Cu, Bi, Mo, Be, Hf, Ta, and W, with a density range between 0.534 and 19.25 kg/m^3. Their exothermic reactions with various substances can form oxides, fluorides, borides, carbides, metallic compounds, and so on. The elemental metals have an energy density range of 2–70 kJ/g or 15–165 kJ/cm^3 when released in oxidation [37,44]. Many reactions between metals and metal compounds, or thermite reactions provide an energy release of 4–6 kJ/g [45]. For air blast, Al is often designated as one of the components within an SRM solid. Al has a large energy density, 32 kJ/g or 86 kJ/cm^3 in oxidation, but also functions as a binder in consolidation of a multi-component granular mixture toward TMD, owing to its high deformability and relatively low melting point.

The rate of energy release from an explosively loaded SRM solid, with respect to augmentation to blast energy, is mostly related to intermetallic reaction within the SRM solid and SRM fragment reaction with oxidizing gases. The latter is more significant and depends not only on the composition but also strongly on the fragment sizes. Fine fragments of an SRM solid can be obtained based on the intrinsic grain-scale properties of dissimilarity and reactivity, for which both composition and mesoscale morphology are important. The selection of individual components includes but is not limited to properties of impedance, ductility, hardness, melting point, particle size, particle shape, and structure as well as reactive properties. If intermetallic reaction within an SRM solid is desired under explosive loading, diffusivity must be considered since intermetallic solid reactions are mostly diffusion-dominant.

To consolidate a granular mixture to a reactive material solid, a variety of techniques can be employed, including mechanical milling [46], vacuum deposition [5], uniaxial pressing, sintering, cold/hot forging and swaging [10,47], cold/hot isostatic pressing (CIP/HIP) [6,8,9,16], high-speed gasdynamic cold-spray deposition (CSD) [15], and explosive forming [14,48]. An SRM solid, which features high mechanical strength and high resistance in sustaining high temperature and pressure environments, requires a consolidation technique capable of achieving TMD with little porosity.

HIP, CSD, and highly compressive forging/swaging, for example, would be appropriate approaches for this purpose and also for large scale production. The final choice of a consolidation technique also relies on its compatibility to the properties of granular materials. For example, hard materials, such as MoO_3, or flakes are in general not well adaptable in CSD [16].

Depending on a consolidation technique, the final composition of an SRM solid may be different from its initial granular mixture. The HIP approach maintains the same ratios of elements as that of the initial mixture which is sealed in a HIP container. However, this is not the same in CSD whereby high-speed particles in the post-nozzle flow partially rebound from the deposition surface. The amount of rebounding particles is different for each component of the mixture, depending on the component properties. Hence, the ratios of elements within the deposited SRM solid are not the same as that in the initial mixture feedstock. It is therefore necessary to quantify the percentage of each element within a formed SRM solid after CSD, using image analysis, energy disperse X-ray (EDX) analysis, etc.

The HIP consolidation employs vacuum degassing and pressing material under conditions of an elevated temperature, at which intermetallic diffusive reaction may take place for certain mixtures (e.g., see Fig. 9). For the same initial mixture, the original species remain without intermetallic reactions in the CSD approach, owing to spraying deposition at cold temperature in the post-nozzle supersonic expansion flow. Hence, examination of final components of a formed SRM solid is needed such as with the help of X-Ray Diffraction (XRD) analysis.

The tensile strength is often more critical than compression strength in applications. Figure 10 provides an example of a tensile curve for a cold-sprayed SRM solid ($\rho_M = 5.5\,g/cm^3$), where the tensile specimen design follows the Metal Powder Industries Federation (MPIF) standard 10. The SRM solid in Fig. 10, practically reaching 100% TMD with a < 1 vol% porosity, shows an ultimate tensile strength (UTS) of 200 MPa. If the SRM solid is heat-treated after CDS, UTS is reduced to 117 MPa after a much greater elongation. Diffusive intermetallic reactions result in chemical bonding

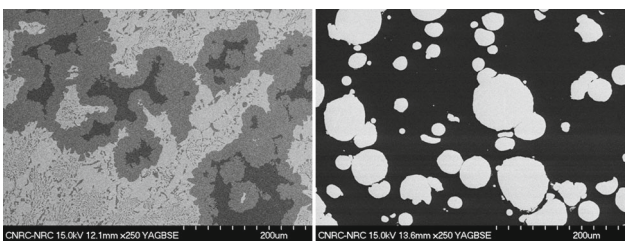

Fig. 9 SEM images for an Al–Zr solid. Left: HIP—degassing and pressing at 500 ° C. Right: CSD

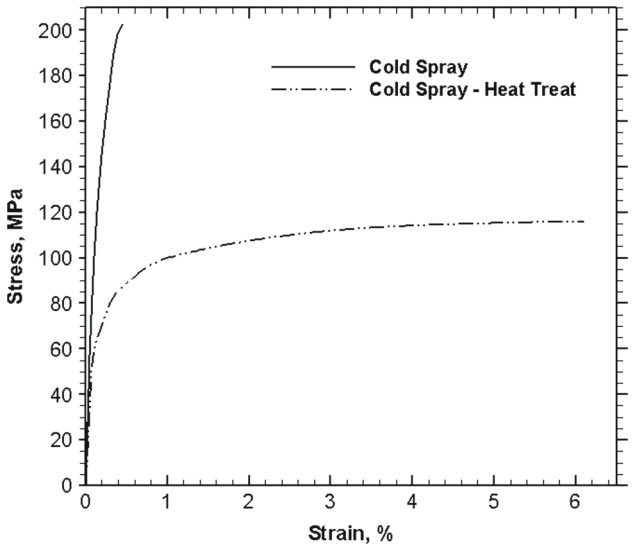

Fig. 10 Tensile curves for a cold spayed SRM solid without and with heat treatment

between the microcomponents, which further improve the tensile strength based on the mechanically bonded components through large plastic strains.

Dynamic mechanical properties of an SRM solid can be measured, for instance, using a Split Hopkinson Pressure Bar or flying plate impact [31,49]. The dynamic compression and shock initiation behavior of an SRM solid can be retrieved from a shock Hugoniot curve obtained from plate impact experiments. Figure 11 displays the shock Hugoniot curves in U_s–U_p and P–V diagrams (U_s: shock velocity; U_p: particle velocity; P: shock pressure; V: shock specific volume), obtained for a cold-sprayed 6Al + CuO solid using a 60 mm gas gun [31]. The SRM solid has a measured density of $3.22\,g/cm^3$ practically reaching the 100% TMD, with a porosity measured to be $< 1\%$, and an UTS in a range of 190–220 MPa [15]. In Fig. 11, a jump occurs near $U_s = 5300\,m/s$ and $P = 18$ GPa, beyond which the Hugoniots shift toward that of the products. It suggests a plausible reaction at this shock pressure level before which the SRM solid withstands a high shock compression. It is noticed in [31] that the acquired emission spectra has not seemed to support a thermite reaction occurring within the shock front that could influence the shock speed.

In the following sections, SRM solids have been mostly made to hollow cylinders with $L/2R_I = 2.15$, where the inner diameter is $2R_I = 33.5$ mm and 76.2 mm to be tested in a cylindrically axisymmetric configuration in the 1.18 m ID, 2.1 m^3 and the 3 m ID, 23 m^3 cylindrical chambers, respectively (see Fig. 7). The SRM hollow cylinders are filled with an explosive mass $C = 0.1$ and 1.2 kg, respectively, and covered by lids, resulting in $M/C = 1.75$–1.78. In the earlier tests, a 101.6-mm-inner-diameter SRM hollow cylinder

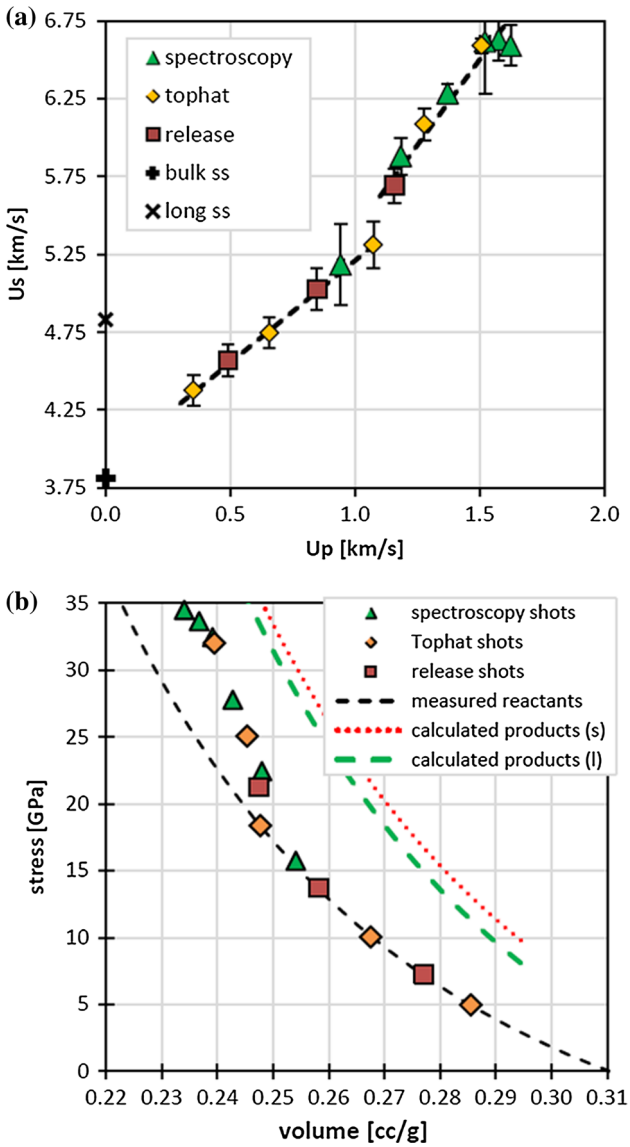

Fig. 11 Hugoniot curves for a 6Al + CuO solid obtained from plate impact tests using a 60 mm gas gun [31]

was also tested in the 23 m^3 chamber. In order for comparison, the baseline 6061-T6 Al casings have been used. To study the effect of detonation pressure on dynamic fragmentation and blast from an SRM solid, two explosives used are: RDX-based composition C4 (HE1: detonation velocity $D_{CJ} = 8000$ m/s and detonation pressure $P_{CJ} = 25$ GPa) and a HMX-based explosive (HE2 : $D_{CJ} = 8500$ m/s and $P_{CJ} = 34$ GPa).

For blast experiments of an SRM solid in a chamber, it is important to have pressure transducers to measure near-field incident blast pressure in order to understand the energy release from the primary SRM fragments. For this purpose, a rigid gauge mount is necessary to record clear and meaningful pressure signals. As shown in Fig. 7, an Endevco piezo-resistive transducer E is set on an in-house designed mount at a radius of $R = 0.39$ m from the charge center in the 2.1 m^3 chamber and a transducer F at $R = 0.89$ m in the 23 m^3 chamber. The wall-mounted transducers, B at $R = 0.59$ m in the 2.1 m^3 chamber and C3 at $R = 1.5$ m in the 23 m^3 chamber, are used to measure the normal-reflected blast and QSP. The chamber is sealed at a local atmospheric air pressure of 92.3–93.7 kPa.

4 Fine fragmentation mechanisms of an SRM solid

4.1 Porosity

High volumetric percentages of porosity provide a fine fragmentation mechanism. High-porosity thick-walled casings have been manufactured from Ti and Zr powder using a sintering technique, to a 73.5-mm-inner-diameter hollow cylinder containing 1 kg of C4 explosive and covered with lids at $M/C = 1.85$. Figure 12 provides high-speed photography results from the sintered Zr casing, with a bulk density of 4.56 g/cm^3 (70% TMD), under explosive loading initiated from the charge top. Fine fragmentation takes place incipiently upon explosive detonation and the resulting fine fragments react promptly in the early phase and continuously as they expand.

Few references from the literature have been found about the effect of porosity on the reaction propagation speed within a reactive or thermite material [30,50,51]. Reference [30] reported that the reaction propagation speed in a confined nanoscale Al–MoO_3 composite decreases from about 1000 to < 600 m/s as the compacted sample density increases from 10 to 48% TMD. This low-density behavior has also been observed in unconfined samples [51] and is consistent with a mechanism dominated by convective flow of hot gas products. As the density increases toward full TMD, the reaction propagation speed is dropped by an order of magnitude as reported for a cold-sprayed microscale Al–CuO unconfined

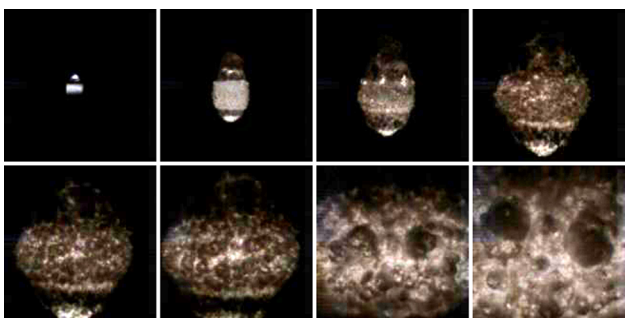

Fig. 12 Prompt fragment reactions upon detonation from a cylindrical 1 kg C4 charge in a 73.5 mm inner diameter, sintered Zr casing ($M/C = 1.85$)

sample [50], suggesting a transition to conductive control at vanishing porosities.

Prompt reaction of fragments from an explosively loaded SRM solid will need mechanisms to generate fine fragments. A high porosity helps fine fragmentation, however, porosity results in a deficit in TMD, thus leading to a low mechanical strength, in particular, to a low tensile strength, which conflicts with the definition of an SRM solid. In order to make a casing possessing high mechanical tensile strength and shock strength, the porosity must be eliminated or limited below a threshold, for example, $<$ 1–2 vol%.

4.2 Structural discontinuity

Fine fragmentation mechanisms of an SRM solid can originate in its inherent mesoscale properties of dissimilarity and reactivity. In a structural discontinuity mechanism [6,7,12,14], the discontinuities in impedance (the product of density and sound speed), hardness, etc., exist at the interfaces between dissimilar granular ingredients within an SRM solid. Near the interfaces, shock dynamics results in local high temperatures, normal/shear stresses, deformation and, later, different accelerations from dissimilar inertia, leading to fine fragments.

The structural discontinuity mechanism is illustrated using a laminate composite, made of 50 μm nickel (Ni) and 150 μm Al layers in cycles, driven by C4 detonation [14]. Nickel has a material density $\rho_M = 8.86\,g/cm^3$ and a sound speed $c = 4646\,m/s$, while the values for Al are $\rho_M = 2.7\,g/cm^3$ and $c = 5350\,m/s$. In this case, shock dynamics at the interfaces of different impedance materials results in non-uniform, high local temperatures and stresses in the Ni–Al laminated layers, as displayed in the wave diagram from a 1D planar simulation of hydrocode Chinook (Martec Ltd.) shown in Fig. 13. As a result of shock reverberating compression between the downstream and upstream Ni layers, the Al peak temperature and pressure increase with layer number as the detonation-induced shock front propagates outwards; late in time, the dissimilar inertia leads to different accelerations. These promote generation of fine fragments whose rapid reaction with air would augment the energy to the blast front. During the shock compression process, in the 1D simulation, the shocked peak temperature in Al layers reaches 1200–1500 K, much lower than the Al melting point at the corresponding peak shock pressures of 45–50 GPa, that is, 2700–3000 K obtained from the high-pressure melting experiments and theory [52,53]. This suggests no significant Ni–Al reaction within the laminate solid during shock compression since the bimetallic diffusion largely depends on Al melting.

A 101.6 mm ID laminate SRM cylinder has been made using explosively forming technique, one 50 μm Ni and two 75 μm Al layers in composite cycles [14]. The SRM casing

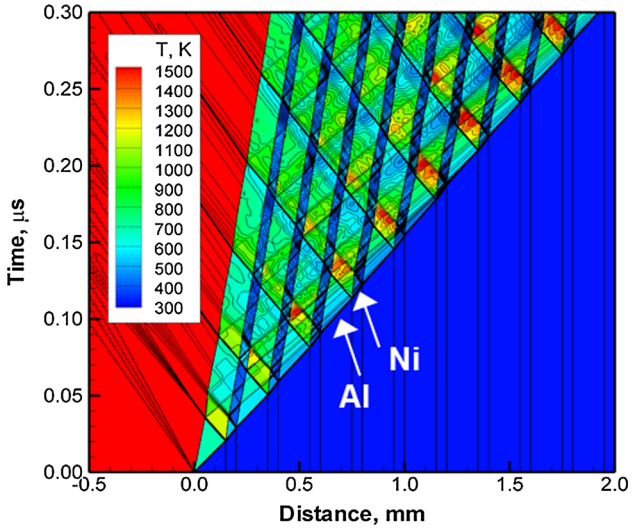

Fig. 13 Wave diagram with temperature (colors) and density (lines from 2 to 11 g/cc) of the early shock reverberating process in 50 μm Ni (blue) and 150 μm Al (green) laminates driven by C4 detonation (left red) [14]

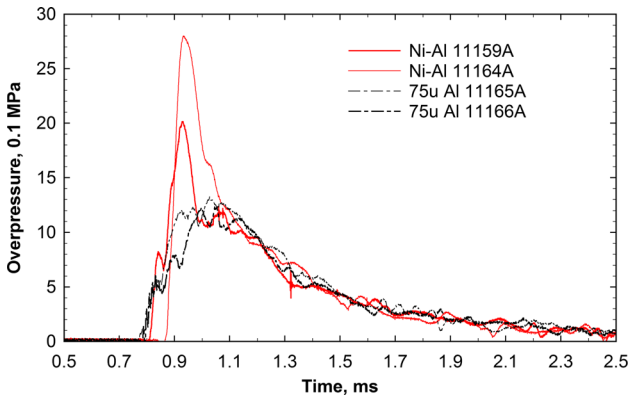

Fig. 14 Normally reflected blast pressure fronts on the wall of a 3 m ID, 23 m^3 cylindrical chamber from 2 kg C4 charges in Ni–Al and 75 μm Al laminate casings ($M/C = 1.75$), respectively

contains 2 kg C4 charge at $M/C = 1.75$, suspended vertically in the center of the 23 m^3 cylindrical chamber and detonated form the charge top. The results, given in Fig. 14, indicate an enhanced blast front pressure in the near field, in comparison with the results from 75 μm Al laminated casings (see Fig. 7 for the normally reflected gauge position). A precursor and primary two-shock front structure, as a typical near-field explosion phenomenon from an SRM-cased charge, is observed for the Al casings and one of the Ni–Al casings; in the latter case, the stronger primary shock is overtaking the precursor.

An increase in density difference between dissimilar materials intensifies mesoscale impedance mismatch within an SRM solid. In a small-scale test configuration [7,8,12], a consolidated 5 g ring from a granular composite of

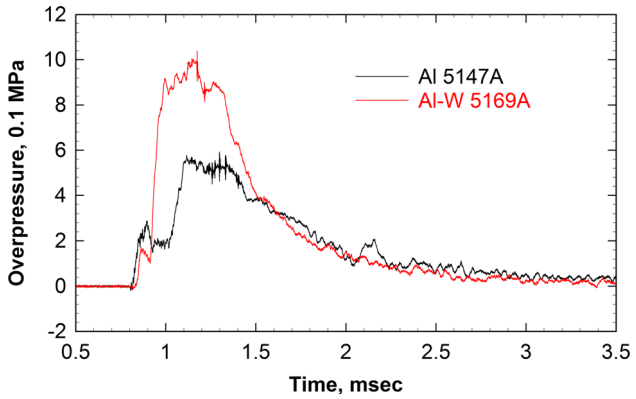

Fig. 15 Normally reflected blast pressure fronts on the wall of a 3 m ID, 23 m^3 cylindrical chamber from a 1.2 kg C4 charge in an Al–W and a baseline Al casing ($M/C = 1.75$), respectively

4.5–7 μm Al and < 44 μm Tungsten (W: $\rho_M = 19.3\,g/cm^3$ and $c = 4060\,m/s$) has provided fragment sizes on the order of a few hundred micrometers under explosive loading. In this case, the 9–15% porosity in the prepared Al–W solids has also helped fine fragmentation. A cold-sprayed 76.2- mm-inner-diameter, thick-walled SRM hollow cylinder, made of granular Al ($d_{50} = 35\,\mu m$) and W (< 53 μm), achieves 100% TMD with a porosity < 1%. The pressure results from this SRM-cased charge (1.2 kg C4 at $M/C = 1.75$) display an expressively enhanced blast front pressure in the near field, compared to the results from the baseline Al casings (Fig. 15).

A higher detonation pressure leads to a stronger shock loading within the SRM solid, thus promoting large discontinuities in strain and strain rate at the grain interfaces and subsequent fine fragmentation.

4.3 Reactive hot spots

In a reactive-hot-spot mechanism, micro- and nano-sized reactive material particles are distributed in a base SRM solid at a fuel-rich equivalence ratio [15,16]. Their intermetallic reactions under explosive loading would create heat and gas products to form mesoscale hot spots, which initiate local fractures leading to fine fragments of the rest of the SRM solid.

Both rapid intermetallic reaction rate and sufficient heat and gas products are necessary for the choice of reactive material in supporting hot spot fine fragmentation. The reactive-hot-spot concept has been tested in blast experiments through distributing micrometric copper oxide particles (CuO, $\rho_M = 6.315\,g/cm^3$) [15], or molybdenum oxide particles (MoO_3, $\rho_M = 4.69\,g/cm^3$) [16] in a particulate Al base and consolidated to a fuel-rich SRM solid. In the MoO_3 example, powders selected are $d_{50} = 35\,\mu m$ atomized Al and ≤ 44 μm MoO_3, and the powder mixture are consolidated by HIP to an SRM solid 10Al + MoO_3. The

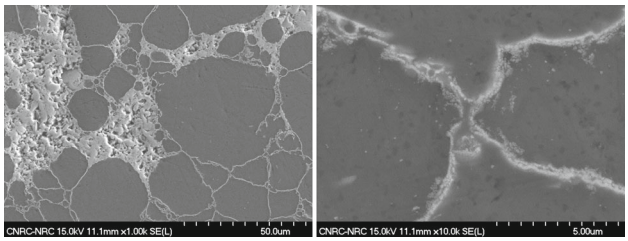

Fig. 16 SEM images for higher magnifications of HIPed 10Al + MoO_3: Al in dark gray and MoO_3 in light gray [16]

SRM solid has a fuel richness $r = 5$ under a global reaction assumption and a bulk density of 3.19 g/cm^3, practically reaching 100% TMD with a 1.46 vol% porosity. It can be seen from the SEM image in Fig. 1 that the MoO_3 is well distributed within the volume. The higher magnifications in Fig. 16 show that the MoO_3 is present in deformed nests with fine Al insides or fine layers between the Al grain boundaries (both inherit from the initial MoO_3 morphology). This microstructure helps an intermetallic reaction controlled by local diffusion between MoO_3 and its neighboring Al, leading to the hot spots. The diffusion-dominant reaction is near stoichiometric in an atomic ratio $N_{Al}/N_{MoO_3} = 2$, resulting in a heat of reaction of 4.703 kJ/g within the hot spot volume and gas products O, O_2, AlO, Al_2O, MoO, MoO_2, etc. at 4600 K, from an equilibrium constant volume explosion calculation at TMD with all phase changes.

The shock initiation pressure for intermetallic reaction within the SRM solid could be another parameter in choosing hot spot reactive material. This initiation threshold in a full TMD SRM solid could be high, for example, 18 GPa or above as indicated in Fig. 11. Under the explosive detonation conditions, the bulk shocked temperature of the SRM solid may not reach the thermite ignition temperature. But shock dynamics on dissimilar Al and MoO_3, local structural discontinuities and any microvoids, shear instability, and plastic deformation can generate intense heat and local high temperatures beyond the ignition threshold of the hot spot material [38,39]. The intermetallic reaction has been confirmed from XRD analysis of the initial SRM fragments with new compounds as the Al–MoO_3 reaction products. Thus, a higher detonation pressure is preferred to increase the hot spot reaction rate and promote hot spot fine fragmentation.

Figure 17 provides both incident and normally reflected pressure results from the explosively loaded 10Al + MoO_3 casing (see Fig. 7 for the gauge positions). The SRM casing contains 100 g C4 explosive at $M/C = 1.78$, suspended in the center of the 2.1 m^3 cylindrical chamber in a cylindrical symmetry configuration. The results clearly indicate enhanced blast front pressure in the near field when compared to that from the baseline Al casings. A further increase in blast peaks is evident through more efficient reactive-

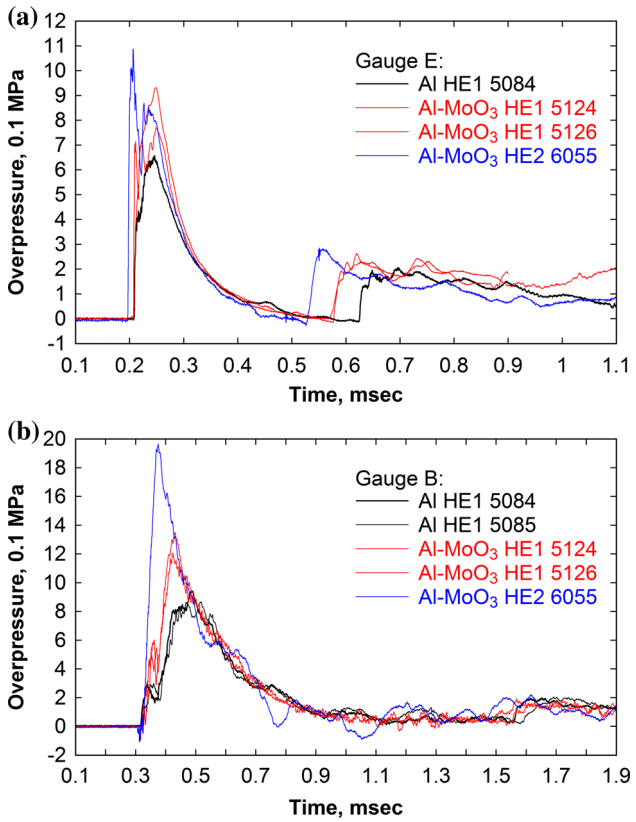

Fig. 17 Blast pressure fronts in a 1.18 m ID, 2.1 m^3 cylindrical chamber from a 100 g charge in $10Al + MoO_3$ and baseline Al casings. **a** At incident gauge E: $R = 39$ cm. **b** On the chamber wall gauge B: $R = 59$ cm

hot-spot fine fragmentation using higher detonation-pressure explosive HE2.

The QSP reached 420–432 kPa for both Al–MoO_3 and baseline Al casings using HE1, measured in late times at 50–100 ms. The same QSP value, together with the blast front results in Fig. 17, indicates that under the same amount of the total energy released (since QSP is proportional to the total energy released in a closed volume), the part of the energy promptly released to enhance the early blast front is significantly more from the Al–MoO_3 casing than that of the Al casing. The QSP is increased to 490 kPa for the Al–MoO_3 casing using HE2.

4.4 Primary fragmentation distribution

In order to optimize the augmentation of the primary and near-field blast energy, a full understanding of the distribution of fine fragment sizes from an explosively loaded SRM solid is important. The recovery of the initial fragments is the key before they have been altered by early reaction or by subsequent impact with surrounding structure.

The collection of fragmentation distribution from a thick cylindrical SRM shell, with fragments including the sizes on the order of $10–10^2$ μm, has been investigated in the 1.18 m ID, 2.1 m^3 cylindrical chamber filled with purified snow of an about 0.4 g/cm^3 packing density, to soft-catch the fragments without secondary fragmentation [34,35]. In the chamber center is an argon-filled charge cavity in a dimension of five times charge diameter and length, which acts both to ensure a full casing expansion and fragmentation at the local atmosphere pressure and to quench any early reaction of SRM fragments in packed snow. After each experiment, the snow containing all fragments is melted, filtered through $a < 1$ μm paper filter, and vacuum-dried in an oven. The sizes of dried fragments are determined using sieves with a distribution of < 37, 37–74, 74–125, 125–420, 420–1000, 1000–2000, 2000–4000, 4000–6300, 6300–9500, and > 9500 μm. The experiments are designed to collect the primary fragments from an SRM cylindrical shell; its top and bottom planar lids are therefore made of mild steel, whose fragments are easily removed by a magnet after a test.

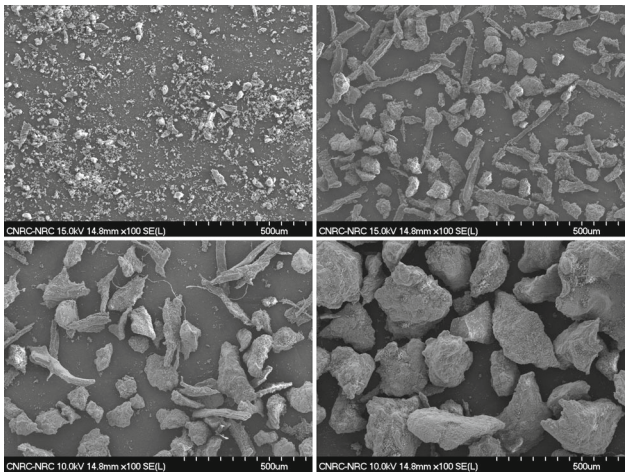

Fig. 18 SEM images for primary fragments of < 37, 37–74, 74–125, and 125–420 μm from SRM solid $10Al + MoO_3$ (#6035*A*) [16]

Figure 18 provides the examples of fine primary fragments from a 33.5- mm-inner-diameter SRM hollow cylinder $10Al + MoO_3$ (described in Sect. 4.3) under the HE2 explosive loading at $M/C = 1.78$. The fragments are in a size range of < 37, 37–74, 74–125, and 125–420 μm. Exceptionally, XRD analysis has been employed for the fine fragments and identified the composition of Al (dominant), MoO_2, Al_2O_3, Mo, $AlMo_3$, Al_3Mo, Al_8Mo_3, etc.. These intermetallic compounds provide a clear evidence for the Al–MoO_3 hot spot thermite reaction within the SRM solid during the detonation shock loading followed by fine fragmentation. Structural discontinuities in impedance, hardness, etc. between Al ($\rho_M = 2.7$ g/cm^3) and MoO_3 ($\rho_M = 4.7$ g/cm^3) plays a secondary role in fine fragmentation.

The purified snow technique provides a full-mass recovery of all primary fragments from an entire cylindrical shell. The obtained primary fragment size distributions are summarized

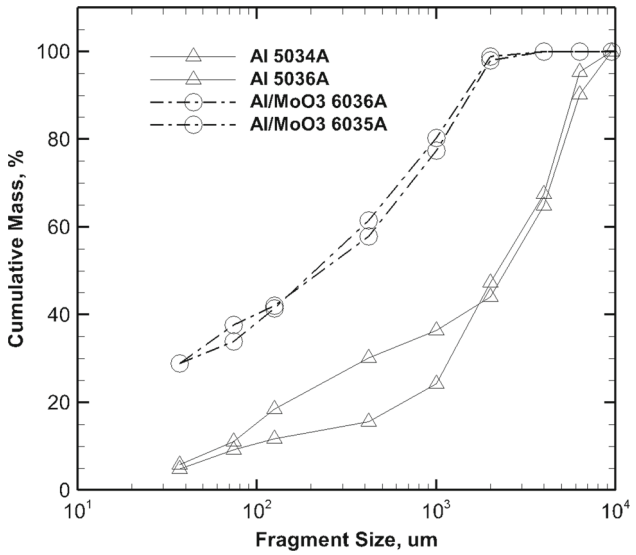

Fig. 19 Primary fragment size distributions from $10Al + MoO_3$ and 6061-T6 Al cylindrical shells [16]

in Fig. 19 for both SRM $10Al + MoO_3$ and baseline 6061-T6 Al cylindrical shell at $M/C = 1.78$. It indicates that the primary fragments in a size range below 125 μm constitute more than 40% mass fraction of the SRM solid, three times that from the pure Al solid.

5 SRM fragment reaction mechanisms

From the viewpoint of explosion performance, the fragment reaction mechanisms can be divided into two categories, namely target impact-induced reaction (IIR) and detonation shock-induced reaction (DSIR) [33–35].

5.1 Target impact-induced reaction

For a primary fragment distribution with a considerable mass fraction comprising large sizes such as fragments from the baseline 6061-T6 Al casing, IIR is dominant as revealed from high-speed photography in Fig. 20. A 33.5- mm-inner-diameter Al casing contains 100 g explosive at $M/C = 1.78$, suspended horizontally in the center of the 2.1 m^3 chamber in a cylindrical symmetry configuration and detonated from the rear end of the charge. The reaction of fragments arises primarily upon impact on the chamber cylindrical wall (see the 5th image at 302 ms), through secondary fragmentation into fine sizes whose combustion significantly increases the reflected blast near the wall. Before impact, only limited fine fragments react after detonation, as shown in the first four frames in Fig. 20 (the four jets at a 90° interval originate from the four screw connections of end lids on the cylindrical casing). The high-speed photography results, together with the

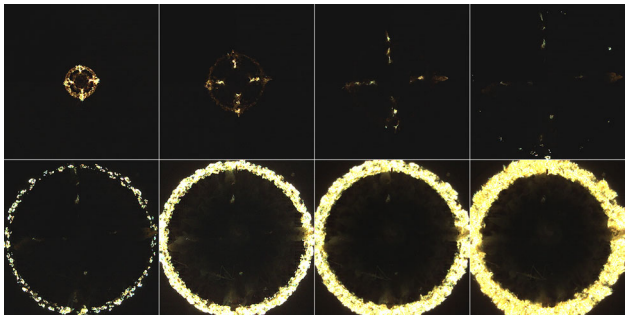

Fig. 20 Al fragment reactions after explosive detonation and upon wall impact from a 33.5 mm inner diameter Al-cased 100 g HE1 charge ($M/C = 1.78$) in the 1.18 ID, 2.1 m^3 chamber. Frames at 52, 105, 184, 289, 302, 315, 328, and 354 μs (#5085) [35]

Al fragment size distribution shown in Fig. 19, further clarify the reasons for the blast performance from the baseline Al casings given in Sect. 2. In summary, little augmentation in free-field primary blast is due to a very limited mass fraction of $\leq$ 100 μm fine primary fragments; a significant increase in internal explosion pressure results mainly from the combustion of the secondary and tertiary fine fragments induced by wall impacts.

5.2 Detonation shock-induced reaction

For a primary fragment distribution with a high mass fraction of micrometric sizes, reaction of these fine fragments can take place promptly following explosive detonation, that is, DSIR as depicted from high-speed photography in Fig. 21. A 33.5- mm-inner-diameter SRM solid casing contains 100 g explosive at $M/C = 1.78$, suspended horizontally in the center of the 2.1 m^3 chamber in a cylindrical symmetry configuration and detonated from the rear end of the charge. The fragments continuously react as the fragment cloud expands, and therefore continuously augment the energy to the propagating primary blast to enhance it in a coherent way. Shortly before the 5th image at 289 ms, the reacting fragments begin to impact the cylindrical wall and rebound, distinguished by an additional brightening boundary at the chamber circumference. The brightening boundary initially moves inwards slowly as the time proceeds from 289 to 368 ms. It then rapidly accelerates and reaches an inward moving speed of 1600 m/s averagely between 368 and 433 ms when crossing the incident burning fragment flow.

A fragment reaction mode in a combination of DRIS and IIR is observed for the $10Al + MoO_3$ SRM hollow cylinder under explosive loading [53]. In that case, a considerable incipient reaction of primary fine fragments appears promptly following detonation before fragments impact the chamber cylindrical wall. The reacting fragments travel and expand faster than that from the baseline Al solid when compared to Fig. 20. These results are consistent with the mass

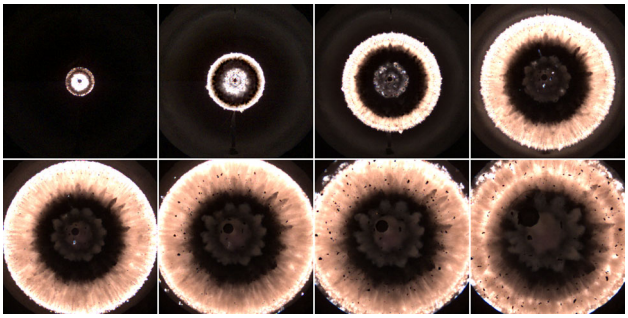

Fig. 21 SRM fragment reactions after explosive detonation from a 33.5-mm-inner-diameter SRM solid-cased 100 g HE2 charge ($M/C = 1.78$) in the 1.18 ID, 2.1 m^3 chamber. Frames at 52, 105, 184, 249, 289, 342, 368, and 420 μs (#6347)

fraction of $\leq 100\,\mu m$ fine primary fragments for both casings given in Fig. 19. IIR takes place as the rest of the larger fragments impact on the wall to generate secondary fine fragments. The augmented primary blast and the secondary fine fragment reactions near the wall together enhance the reflected blast peak, as indicated in the blast pressure results described in Sect. 4.3.

6 Conclusions

Structural reactive material, as one of the open areas in material science, is consolidated from a mixture of micro- or nanometric energetic metals and metal compounds to the mixture TMD. An SRM therefore possesses both bulk continuum solid properties (high energy, density, and mechanical strength) and mesoscale properties of reactivity and dissimilarity (i.e., chemical, physical, and structural discontinuities at particle interfaces). These properties may have a great potential in various applications beyond current considerations.

When SRM is applied to an explosive system, it supplements both significant energy and high mechanical strength and temperature sustenance. In order to promptly release energy from an SRM solid to augment air blast, mechanisms for generating fine primary fragments are needed particularly from a thick SRM casing under explosive loading. High volumetric porosity promotes fine fragmentation but results in a deficit in TMD, thus leading to a low tensile strength, which conflicts with the definition of an SRM solid. In order for a high mechanical tensile strength and shock strength, the density of an SRM solid must reach full TMD with porosity to be excluded ($<$ 1–2 vol% in practice).

From the intrinsic mesostructure of dissimilarity and reactivity of a full-TMD SRM solid, fine fragmentation mechanisms have been proposed. One of the fine fragmentation mechanisms uses mesoscale structural discontinuities within an SRM solid that is comprised of multiple dissimilar materials. Shock dynamics at the interfaces of different impedance and hardness materials results in non-uniform, high local temperatures, stresses, and deformation, and later in time the dissimilar inertia causes different accelerations, thus leading to local fracture and fine fragments. Another fine fragmentation mechanism uses a reactive-hot-spot concept, through distributing micro- or nano-sized reactive materials in a fuel-rich SRM solid. Intermetallic or thermite reactions of these fine materials under explosive loading create heat and gas products to form mesoscale hot spots that initiate local fractures leading to fine fragments of the rest of the SRM solid.

Both fine fragmentation mechanisms have been successfully demonstrated through dynamic fragmentation and blast performance experiments, using various SRM solids, made of a variety of compositions, powder morphologies, and consolidation technologies essentially reaching full TMD with little porosity. For both mechanisms, high detonation pressures are critical in generating large discontinuities in strain and strain rate at the grain interfaces. As for the reactive-hot-spot fine fragmentation mechanism, the high detonation shock also helps initiate intermetallic reaction within an SRM solid. In addition, a high intermetallic reaction rate and sufficient gas products are necessary for the choice of reactive material in favoring hot spot fine fragmentation. A purified snow technique has been developed and facilitates a full-mass recovery of all primary fragments, including the sizes on the order of $10–10^2\,\mu m$, from an entire cylindrical shell. The full-mass recovery of primary fragments before they have been altered by early reaction or by subsequent impact with surrounding structures is vital in deriving a complete fragment size distribution for the understanding of energy release processes from an explosively loaded SRM solid.

From the viewpoint of blast performance, the fragment reaction mechanisms may be divided into two categories, namely detonation shock-induced reaction (DSIR) and target impact-induced reaction (IIR). Experiments indicate that for a fragment distribution with a high mass fraction comprising large sizes, IIR is dominant and the reaction of fragments arises primarily upon impact on the chamber wall through resulting secondary fine fragment combustion to enhance the reflected blast near the wall. For a distribution with a large mass fraction of micrometric size fragments, DSIR prevails and the reaction of the primary fine fragments takes place promptly following explosive detonation and continues as the fragment cloud expands, thus continuously augmenting the energy to the primary blast in the near field. Combination between DSIR and IIR can be achieved through engineering an SRM solid for an appropriate fragmentation distribution in both fine and large sizes.

While the discussions have mostly been based on the explosion and blast performance, more fundamental studies would be required for full TMD SRM solids in the areas of

shock dynamics in microstructures, intermetallic reaction, fragmentation, dense reactive particle flow, heterogeneous blast, and confinement effects. Studies on shock and impact dynamic behavior and reaction of full TMD SRM solids are necessary to understand the detailed mechanisms of SRM fine fragmentation, initiation, and reaction under explosive loading.

Acknowledgements The author is grateful to B. Eichelbaum, K. Mudri, R. Stallmann, R. Laing, L. Gagne, R. Finlay, K. Baker, M., Radulescu, M. Gauthier, C.V. Cojocaru, R. Ripley, L. Donahue, K. Kim, W. Wilson, and technical staff from the Suffield Field Operations Section for their input into the work described above.

References

1. Batsanov, S.: Solid-phase reactions in shock waves: Kinetic studies and mechanism. Combust. Explos. Shock Waves **32**(1), 102–113 (1996). doi:10.1007/BF01992198
2. Kuznetsov, N.: Detonation and gas-dynamic jumps during phase transformations in metastable compounds. Zh. Eksp. Teor. Fiz. **49**, 1526–1531 (1965)
3. Merzhanov, A., Gordopolov, Y.A., Trofimov, V.: On the possibility of gasless detonation in condensed systems. Shock Waves **6**, 157–159 (1996). doi:10.1007/BF02510996
4. Thadhani, N.: Shock-induced and shock-assisted solid-state chemical reactions in powder mixtures. J. Appl. Phys. **76**(4), 2129–2138 (1994). doi:10.1063/1.357624
5. Adams, D.: Reactive multilayers fabricated by vapor deposition: A critical review. Thin Solid Films **576**, 98–128 (2015). doi:10.1016/j.tsf.2014.09.042
6. Chiu, P.-H., Nesterenko, V.F.: Processing and mechanical properties of novel Al–W composites with ordered mesostructure. J. Compos. Mater. **50**(28), 4015–4022 (2016). doi:10.1177/0021998316630802
7. Chiu, P.-H., Lee, C.-W., Nesterenko, V.F.: Processing and dynamic testing of Al/W granular composites. Shock Compression of Condensed Matter–2011. AIP Conf. Proc. **1426**, 737–740 (2012). doi:10.1063/1.3686384
8. Chiu, P.-H., Olney, K.L., Benson, D.J., Braithwaite, C., Collins, A., Nesterenko, V.F.: Dynamic fragmentation of Al-W granular rings with different mesostructures. J. Appl. Phys. **121**(4), 045901 (2017). doi:10.1063/1.4973730
9. Chiu, P.-H., Vecchio, K.S., Nesterenko, V.F.: Dynamic compressive strength and mechanism of failure of Al–W fiber composite tubes with ordered mesostructure. Int. J. Impact Eng **100**, 1–6 (2017). doi:10.1016/j.ijimpeng.2016.10.003
10. Gibbins, J., Stover, A., Krywopusk, N., Woll, K., Weihs, T.: Properties of reactive Al:Ni compacts fabricated by radial forging of elemental and alloy powders. Combust. Flame **162**(12), 4408–4416 (2015). doi:10.1016/j.combustflame.2015.08.003
11. Marín, L., Nanayakkara, C.E., Veyan, J.-F., Warot-Fonrose, B., Joulie, S., Estève, A., Tenailleau, C., Chabal, Y.J., Rossi, C.: Enhancing the reactivity of Al/CuO nanolaminates by Cu incorporation at the interfaces. ACS Appl. Mater. Interfaces **7**(22), 11713–11718 (2015). doi:10.1021/acsami.5b02653
12. Nesterenko, V.F., Chiu, P.-H., Braithwaite, C., Collins, A., Williamson, D.M., Olney, K.L., Benson, D., McKenzie, F.: Dynamic behavior of particulate/porous energetic materials. Shock Compression of Condensed Matter–2011. AIP Conf. Proc. **1426**, 533–538 (2011)
13. Zhang, F., Donahue, L., Wilson, W.H.: The effect of charge structural-reactive-metal cases on air blast. In: Proceedings of 14th Detonation Symposium, Coeur d'Alene, ID, pp. 2–12 (2010)
14. Zhang, F., Ripley, R., Wilson, W.: Air blast characteristics of laminated Al and Ni-Al casings. Shock Compression of Condensed Matter–2011. AIP Conf. Proc. **1426**, 275–278 (2012). doi:10.1063/1.3686272
15. Zhang, F., Bacciochini, A., Jodoin, B., Radulescu, M., Ripley, R.: A hot spot concept to enhance fragmentation of structural-reactive-material casings. In: Proceedings of 15th Detonation Symposium, San Francisco, CA, pp. 1356–1366 (2014)
16. Zhang, F., Gauthier, M., Cojocaru, C.V.: Dynamic fragmentation and blast from a reactive material solid. Propellants Explos. Pyrotech. **42**(9), 1072–1078 (2017). doi:10.1002/prep.201700065
17. Filler, W.: The influence of reactive cases on airblast from high explosives. In: Proceedings of 8th Detonation Symposium, Albuquerque, NM, pp. 86–194 (1985)
18. Beckstead, M.: Correlating aluminum burning times. Combust. Explos. Shock Waves **41**(5), 533–546 (2005). doi:10.1007/s10573-005-0067-2
19. Frost, D.L., Zhang, F.: The nature of heterogeneous blast explosives. In: Proceedings of the 19th International Symposium on Military Aspects of Blast and Shock, Calgary, Canada, pp. 1–51 (2006)
20. Frost, D.L., Goroshin, S., Levine, J., Ripley, R., Zhang, F.: Critical conditions for ignition of aluminum particles in cylindrical explosive charges. Shock Compression of Condensed Matter–2005. AIP Conf. Proc. **845**, 972 (2006). doi:10.1063/1.2263484
21. Zhang, F.: Detonation of gas–particle flow. In: Zhang, F. (ed.) Shock Wave Science and Technology Reference Library, vol. 4, pp. 87–168. Springer, Berlin (2009). doi:10.1007/978-3-540-88447-7_2
22. Zhang, F., Gerrard, K., Ripley, R.C.: Reaction mechanism of aluminum–particle–air detonation. J. Propuls. Power **25**(4), 845 (2009). doi:10.2514/1.41707
23. Clemenson, M.D., Johnson, S., Krier, H., Glumac, N.: Explosive initiation of various forms of Ti/2B reactive materials. Propellants Explos. Pyrotech. **39**(3), 454–462 (2014). doi:10.1002/prep.201300114
24. Herbold, E., Nesterenko, V., Benson, D., Cai, J., Vecchio, K., Jiang, F., Addiss, J., Walley, S., Proud, W.: Particle size effect on strength, failure, and shock behavior in polytetrafluoroethylene–Al–W granular composite materials. J. Appl. Phys. **104**(10), 103903 (2008). doi:10.1063/1.3000631
25. Joshi, V.S.: Process for making polytetrafluoroethylene–aluminum composite and product made. US Patent 6,547,993 (2003)
26. Nielson, D., Truitt, R., Poore, R., Ashcroft, B.: Reactive material compositions for shot shells ammunition consisting of metal fuels, inorganic oxidants, epoxy resins, and fluoropolymer binders. US20070272112A1 (2007)
27. Grady, D.: The spall strength of condensed matter. J. Mech. Phys. Solids **36**(3), 353–384 (1988). doi:10.1016/0022-5096(88)90015-4
28. Kipp, M., Grady, D.: Dynamic fracture growth and interaction in one dimension. J. Mech. Phys. Solids **33**(4), 399–415 (1985). doi:10.1016/0022-5096(85)90036-5
29. Dutro, G., Yetter, R., Risha, G., Son, S.: The effect of stoichiometry on the combustion behavior of a nanoscale Al/MoO_3 thermite. Proc. Combust. Inst. **32**(2), 1921–1928 (2009). doi:10.1016/j.proci.2008.07.028
30. Sanders, V.E., Asay, B.W., Foley, T.J., Tappan, B.C., Pacheco, A.N., Son, S.F.: Reaction propagation of four nanoscale energetic composites. J. Propuls. Power **23**(4), 707–714 (2007). doi:10.2514/1.26089
31. Neel, C., Lacina, D., Johnson, S.: Laser interferometry and emission spectroscopy measurements of cold-sprayed copper thermite shocked to 35 GPa. ShockCompression of Condensed Matter—

2015. AIP Conf. Proc. **1793**, 040017 (2017). doi:10.1063/1.4971511
32. Williams, R.A., Patel, J.V., Ermoline, A., Schoenitz, M., Dreizin, E.L.: Correlation of optical emission and pressure generated upon ignition of fully-dense nanocomposite thermite powders. Combust. Flame **160**(3), 734–741 (2013). doi:10.1016/j.combustflame.2012.11.021
33. Kim, K., Wilson, W., Quintana, J., Roybal, J., Rocco, J., Watry, C., Brown, M., Zahrah, T., Glumac, N., Clemenson, M.: Detonation initiated chemical reactions in structural energetic materials. In: Proceedings of 15th Detonation Symposium, San Francisco, CA, pp. 1347–1355 (2014)
34. Wilson, W.H., Zhang, F., Kim, K.: Fine fragmentation distribution from structural reactive material casings under explosive loading. Shock Compression of Condensed Matter—2015. AIP Conf. Proc. **1793**, 040037 (2017). doi:10.1063/1.4971531
35. Zhang, F., Gauthier, M., Cojocaru, C.: Sub-fragmentation of structural reactive material casings under explosion. Shock Compression of Condensed Matter—2015. AIP Conf. Proc. **1793**, 040038 (2015). doi:10.1063/1.4971532
36. Grady, D.: Fragmentation of Rings and Shells: The Legacy of N.F. Mott. Springer, Berlin (2007). doi:10.1007/b138675
37. Hastings, D.L., Dreizin, E.L.: Reactive structural materials: Preparation and characterization. Adv. Eng. Mater. (2017). doi:10.1002/adem.201700631
38. Nesterenko, V.: Dynamics of Heterogeneous Materials. Springer, New York (2013). doi:10.1007/978-1-4757-3524-6
39. Thadhani, N.N.: Shock-induced chemical reactions and synthesis of materials. Prog. Mater Sci. **37**(2), 117–226 (1993). doi:10.1016/0079-6425(93)90002-3
40. Elek, P., Jaramaz, S.: Modeling of fragmentation of rapidly expanding cylinders. Theor. Appl. Mech. **32**(2), 113–130 (2005). doi:10.2298/TAM0502113E
41. Hutchinson, M.D.: The escape of blast from fragmenting munitions casings. Int. J. Impact Eng. **36**(2), 185–192 (2009). doi:10.1016/j.ijimpeng.2008.05.002
42. Zhang, F., Wilson, W.H.: Reaction of fragments from cased explosive charges. In: Proceedings of the 20th International Symposium on Military Aspects of Blast and Shock, Oslo, Norway, pp. 1–9 (2008)
43. Ripley, R., Donahue, L., Zhang, F.: Fragmentation of metal particles during heterogeneous explosion. Shock Waves **25**(2), 151–167 (2015). doi:10.1007/s00193-015-0552-9
44. Chase, M.W.: NIST-JANAF thermochemical tables for oxygen fluorides. J. Phys. Chem. Ref. Data **25**(2), 551–603 (1996). doi:10.1063/1.555992
45. Fischer, S.H., Grubelich, M.: Theoretical energy release of thermites, intermetallics, and combustible metals. Technical report SAND-98-1176C, Sandia National Labs, Albuquerque, NM, USA (1998). doi:10.2172/658208
46. Dreizin, E.L., Schoenitz, M.: Mechanochemically prepared reactive and energetic materials: a review. J. Mater. Sci. (2017). doi:10.1007/s10853-017-0912-1
47. Marquez, A.M., Braithwaite, C.H., Weihs, T.P., Krywopusk, N.M., Gibbins, D.J., Vecchio, K.S., Meyers, M.A.: Fragmentation and constitutive response of tailored mesostructured aluminum compacts. J. Appl. Phys. **119**(14), 145903 (2016). doi:10.1063/1.4945813
48. Prümmer, R.: Explosivverdichtung pulvriger Substanzen: Grundlagen, Verfahren, Ergebnisse, vol. 7. Springer, Heidelberg (2013). doi:10.1007/978-3-642-82903-1
49. Proud, W.G., Williamson, D.M., Field, J.E., Walley, S.M.: Diagnostic techniques in deflagration and detonation studies. Chem. Cent. J. **9**(1), 52 (2015). doi:10.1186/s13065-015-0128-x
50. Bacciochini, A., Maines, G., Poupart, C., Akbarnejad, H., Radulescu, M., Jodoin, B., Zhang, F., Lee, J.: Study of thermite mixture consolidated by the cold gas dynamic spray process. J. Phys. Conf. Ser. **500**, 220–225 (2014). doi:10.1088/1742-6596/500/5/052003
51. Pantoya, M.L., Granier, J.J.: Combustion behavior of highly energetic thermites: Nano versus micron composites. Propellants Explos. Pyrotech. **30**(1), 53–62 (2005). doi:10.1002/prep.200400085
52. Lees, J., Williamson, B.: Combined very high pressure/high temperature calibration of the tetrahedral anvil apparatus, fusion curves of zinc, aluminium, germanium and silicon to 60 kilobars. Nature **208**(5007), 278–279 (1965). doi:10.1038/208278a0
53. Moriarty, J.A., Young, D.A., Ross, M.: Theoretical study of the aluminum melting curve to very high pressure. Phys. Rev. B **30**(2), 578 (1984). doi:10.1103/PhysRevB.30.578